Wave patterns in thin film flows

B. Scheid*, C. Ruyer-Quil** & P. Manneville***

*Chimie-Physique E.P., Université Libre de Bruxelles C.P. 165/62, Avenue F.D. Roosevelt, 50 - 1050 Bruxelles
**Laboratoire FAST, Université Paris-Sud – UMR CNRS 7608, Campus universitaire, 91405 Orsay, France
***LadHyX – UMR CNRS 7646, École polytechnique, 91128 Palaiseau, France
bscheid@ulb.ac.be, ruyer@fast.u-psud.fr, paul.manneville@ladhyx.polytechnique.fr

Abstract— **The application of a systematic strategy to the problem of falling liquid films is shown to lead to systems of equations of reduced dimensionality that capture the physical mechanisms quite faithfully, helping us to enlighten the observed dynamics by isolating the important physical effects. Additionally, a regularization procedure applied in the approach pushes away the validity range of a consistent three-field modeling of film flows in parameter space by reducing the degrees of the dangerous nonlinear terms. Having at one's disposal reliable low-dimension models, one is able to undergo a systematic numerical analysis at low cost (in terms of CPU time). Consequently, complex wave patterns such as herringbone patterns, synchronously deformed fronts, V-shape solitary waves observed in various experimental data can be recovered. In this paper, we specifically compare our model to recent and well-controlled experiments by Park & Nosoko [AIChE J., 49, 2715 (2003)].**

Keywords— **Hydrodynamic instabilities, falling films, Solitary waves**

I. Introduction

Thin films flowing down inclines have a rich dynamics extensively studied for a long time since Kapitza's experimental and theoretical pioneering works at the end of the forties [1]. Besides their importance for engineering applications (e.g. evaporators or chemical reactors), their interest mainly stems from the fact that their evolution is amenable to thorough theoretical analysis. This situation happens mostly due to the two-dimensional, long-wavelength, supercritical character of the primary instability mode. Thickness modulations which develop over initially uniform films are usually spanwise homogeneous and slowly varying both in time and in space, which allows gradient expansions on which relies the lubrication approximation. The approach is thus similar to that followed in the study of boundary layers and deep analogies can be found in the transition to turbulence of each system, especially at the level of secondary instabilities.

This paper, the details of which are given in [2], is devoted to the study of the three-dimensional (noted 3D) wavy dynamics of film flows, up to moderate Reynolds numbers, i.e. where single-variable models [3–5] are known to fail, contrary to multiple-variable models [6, 7].

For a film flowing down a vertical plate, experiments show evidence of a 3D wavy regime after inception, succeeding to a regime of spanwise uniform waves —i.e. 2D waves— resulting from the primary instability of the uniform film flow. The final state of the film corresponds to a disordered dynamics dominated by 3D solitary waves, or "3D soliton gas" [7]. Recent experimental results by Park & Nosoko [8] give a clear picture of the transition from 2D to 3D dynamics when the Reynolds numbers is increased. These authors imposed a low frequency forcing on the entrance flow rate and spanwise modulations at the inlet with the help of an array of needles. For films of water on a vertical wall, Park & Nosoko distinguished two different scenarios for the 3D instabilities of the fast γ_2 waves[1] depending on the Reynolds number. At R below approximately 40, regular spanwise forcing of the waves led to low-level spanwise modulations whereas at R above 40, the waves broke into horseshoe-like solitary waves having curved fronts and long oblique legs.

In section II, we derive our three-equation regularized model. Section III is dedicated to the numerical simulations of the regularized model in the experimental conditions of Park & Nosoko [8]. Concluding remarks and perspectives are presented in section IV.

II. Two-dimensional modeling of three-dimensional film flows

The flow of a Newtonian liquid down an inclined plane is considered. We look for two-dimensional equations in the streamwise (x) and spanwise (z) coordinates that mimic the full 3D motion of the fluid (y being the cross-stream coordinate). Our approach is based on the long-wave approximation which ensures slow time and space modulations of the basic flat film solution (Nusselt flow), by writing that partial derivatives $\partial_t, \partial_x, \partial_z$ are all of order ϵ, with $\epsilon \ll 1$. The first step consists in the elimination of the pressure in the Navier–Stokes equations truncated at $O(\epsilon^3)$, leading to the second-order boundary layer equations, which read

$$\begin{aligned}
&\delta\left[\partial_t u + \partial_x(u^2) + \partial_y(uv) + \partial_z(uw)\right] = \\
&1 + \partial_{yy}u - \zeta\,\partial_x h + \partial_{xxx}h + \partial_{xzz}h \\
&+\eta\left[2\partial_{xx}u + \partial_{zz}u + \partial_{xz}w - \partial_x(\partial_y v\big|_h)\right] , \qquad (1a)\\
&\delta\left[\partial_t w + \partial_x(uw) + \partial_y(vw) + \partial_z(w^2)\right] = \\
&\partial_{yy}w - \zeta\,\partial_z h + \partial_{xxz}h + \partial_{zzz}h \\
&+\eta\left[2\partial_{zz}w + \partial_{xx}w + \partial_{xz}u - \partial_z(\partial_y v\big|_h)\right] , \qquad (1b)\\
&\partial_x u + \partial_y v + \partial_z w = 0\,, \qquad (1c)
\end{aligned}$$

where $h = h(x, z, t)$ is the local film thickness, and (u, v, w) the streamwise, cross-stream and spanwise components of the velocity field. Equations (1a) and (1b) correspond to the streamwise and spanwise momentum balances, respectively, and (1c) is the continuity equation. This set of equations is completed by the no-slip condition at the wall $y = 0$:

$$u = v = w = 0\,, \qquad (1d)$$

[1] Following Chang's terminology [9], γ_2 waves refer to positive waves while γ_1 waves to negative ones.

and the x and z directions of the stress balance at the free surface $y = h$:

$$\partial_y u = \eta\left[\partial_z h(\partial_z u + \partial_x w) + 2\partial_x h(2\partial_x u + \partial_z w) - \partial_x v\right], \quad (1e)$$
$$\partial_y w = \eta\left[\partial_x h(\partial_z u + \partial_x w) + 2\partial_z h(2\partial_z w + \partial_x u) - \partial_z v\right]. \quad (1f)$$

The dimensionless numbers in (1) are, respectively, the reduced Reynolds number, the reduced slope and the viscous diffusion parameter, defined as:

$$\delta = \frac{(3R)^{11/9}}{\Gamma^{1/3}}, \quad \zeta = \frac{\cot\beta(3R)^{2/9}}{\Gamma^{1/3}} \quad \text{and} \quad \eta = \frac{(3R)^{4/9}}{\Gamma^{2/3}}.$$

These numbers are based on the inclination $\cot\beta$ and the usual Reynolds and Kapitza numbers in turn defined as

$$R = \frac{g\sin\beta h_{\rm N}^3}{3\nu^2} \qquad \text{and} \qquad \Gamma = \frac{\sigma}{\rho\nu^{4/3}(g\sin\beta)^{1/3}},$$

with β the inclination angle from the horizontal, g the gravity acceleration, $h_{\rm N}$ the thickness of the uniform film, ν the kinematic viscosity and σ the surface tension.

Second-order terms gathered under η in system (1) account for streamwise viscous diffusion. These equations are symmetric under the exchange $\{u \leftrightarrow w,\ x \leftrightarrow z\}$, except for the gravity term scaled to unity in (1a). The flat film solution is a parallel flow with no spanwise component, i.e. $w = 0$. A valid approach is therefore to consider w of order ϵ, with the meaning that spanwise flows are triggered by the modulations of the free surface. Ruyer-Quil & Manneville [10] used this assumption to simplify the cumbersome system of equations which models the 3D flow dynamics. However least degeneracy considerations about the continuity equation (1c) suggest us to take w of order unity, and this is the approach we will take below.

Following the same procedure as for the 2D case [10], one obtains that six independent fields are needed to account for the velocity components at second order: the streamwise and spanwise flow rates $q = \int_0^h u\,{\rm d}y$ and $p = \int_0^h w\,{\rm d}y$, and four corrections s_1, s_2, r_1 and r_2 corresponding to the polynomial test functions g_1 and g_2 and accounting for the deviations of the velocity profiles away from the zeroth-order parabolic profile g_0 (polynomials g_i are defined in appendix A). The boundary layer equations are then averaged using the Galerkin method by writing residuals $\langle E_\parallel, g_i\rangle$ and $\langle E_\perp, g_i\rangle$ where $\langle f, g\rangle = \int_0^h f\,g\,{\rm d}y$, while $E_\parallel$ and $E_\perp$ refer to the streamwise (1a) and spanwise (1b) momentum balances, respectively. These residuals yield a system of six evolution equations for h, q, s_1, s_2, p, r_1 and r_2, completed with the mass balance obtained through integration of (1c) across the layer depth:

$$\partial_t h = -\partial_x q - \partial_z p\,. \quad (2)$$

This system is called the *complete model* in the following. Here, we follow a regularization procedure that aims at reducing the complete model to only three equations for h, q and p. First-order expressions of the fields s_1, s_2, r_1 and r_2 are readily obtained from the truncation at order ϵ of the residuals corresponding to the weights g_1 and g_2. Substitution of these expressions in the first residuals $\mathcal{R}_{0,\parallel} = \langle E_\parallel, g_0\rangle$ and $\mathcal{R}_{0,\perp} = \langle E_\perp, g_0\rangle$ produces second-order inertia terms, formally written as $\mathcal{R}_{0,\parallel}^{(2),\delta}$ and $\mathcal{R}_{0,\perp}^{(2),\delta}$. These terms contain high-order nonlinearities that we next kill by adjusting algebraic preconditioners. So residuals $\mathcal{R}_{0,\parallel}$ and $\mathcal{R}_{0,\perp}$ are searched in the form $\mathcal{G}_\parallel^{-1}\mathcal{F}_\parallel$ and $\mathcal{G}_\perp^{-1}\mathcal{F}_\perp$ where $\mathcal{F}_\parallel$ and $\mathcal{F}_\perp$ correspond to the expressions of the residuals $\mathcal{R}_{0,\parallel}$ and $\mathcal{R}_{0,\perp}$ when a parabolic velocity profile is assumed, i.e. when corrections s_i and r_i are neglected. Isolating inertia terms, we thus set:

$$\begin{aligned}\mathcal{G}_\parallel\left(\mathcal{R}_{0,\parallel}^{(1),\delta} + \mathcal{R}_{0,\parallel}^{(2),\delta}\right) &= \mathcal{R}_{0,\parallel}^{(1),\delta}\\ \mathcal{G}_\perp\left(\mathcal{R}_{0,\perp}^{(1),\delta} + \mathcal{R}_{0,\perp}^{(2),\delta}\right) &= \mathcal{R}_{0,\perp}^{(1),\delta},\end{aligned} \quad (3)$$

where superscripts refer to first-order and second-order inertia terms. Zeroth-order expressions of the flow rates $q = h^3/3 + O(\epsilon)$ and $p = O(\epsilon)$, i.e. the gravity-oriented (base) flow, are next invoked to reduce the degree of nonlinearities of the regularization factors $\mathcal{G}_\parallel$ and $\mathcal{G}_\perp$. Consequently, the inertia terms $\mathcal{R}_{0,\perp}^{(2),\delta}$ induced by deviations of the spanwise velocity field from the parabolic profile appear asymptotically at order ϵ^3. So that we merely get $\mathcal{G}_\perp = 1 + O(\epsilon^2)$. Similarly, the asymptotic expression of $\mathcal{R}_{0,\parallel}^{(2),\delta}$ corresponds exactly to the one obtained for a spanwise independent flow. Hence we have

$$\mathcal{G}_\perp \equiv 1 \quad \text{and} \quad \mathcal{G}_\parallel \equiv \left[1 - \frac{\delta}{70}q\partial_x h\right]^{-1}. \quad (4)$$

Completing (2), the 3D *regularized model* then reads:

$$\begin{aligned}
&\delta\,\partial_t q = \delta\left[\frac{9}{7}\frac{q^2}{h^2}\partial_x h - \frac{17}{7}\frac{q}{h}\partial_x q\right] \quad (5a)\\
&+\left\{\frac{5}{6}h - \frac{5}{2}\frac{q}{h^2} + \delta\left[-\frac{8}{7}\frac{q\partial_z p}{h} - \frac{9}{7}\frac{p\partial_z q}{h} + \frac{9}{7}\frac{qp\partial_z h}{h^2}\right]\right.\\
&+\eta\left[4\frac{q\,(\partial_x h)^2}{h^2} - \frac{9}{2}\frac{\partial_x q\partial_x h}{h} - 6\frac{q\partial_{xx}h}{h} + \frac{9}{2}\partial_{xx}q\right.\\
&+\frac{13}{4}\frac{p\partial_x h\partial_z h}{h^2} - \frac{\partial_z q\partial_z h}{h} - \frac{43}{16}\frac{\partial_x p\partial_z h}{h} - \frac{13}{16}\frac{\partial_z p\partial_x h}{h}\\
&\left.\left.+\frac{3}{4}\frac{q\,(\partial_z h)^2}{h^2} - \frac{23}{16}\frac{q\partial_{zz}h}{h} - \frac{73}{16}\frac{p\partial_{xz}h}{h} + \partial_{zz}q + \frac{7}{2}\partial_{xz}p\right]\right.\\
&\left.-\frac{5}{6}\zeta h\,\partial_x h + \frac{5}{6}h\,(\partial_{xxx} + \partial_{xzz})\,h\right\}\left(1 - \frac{\delta}{70}q\partial_x h\right)^{-1},\\
&\delta\,\partial_t p = \delta\left[\frac{9}{7}\frac{p^2}{h^2}\partial_z h - \frac{17}{7}\frac{p}{h}\partial_z p\right] \quad (5b)\\
&-\frac{5}{2}\frac{p}{h^2} + \delta\left[-\frac{8}{7}\frac{p\partial_x q}{h} - \frac{9}{7}\frac{q\partial_x p}{h} + \frac{9}{7}\frac{qp\partial_x h}{h^2}\right]\\
&+\eta\left[4\frac{p\,(\partial_z h)^2}{h^2} - \frac{9}{2}\frac{\partial_z p\partial_z h}{h} - 6\frac{p\partial_{zz}h}{h} + \frac{9}{2}\partial_{zz}p\right.\\
&+\frac{13}{4}\frac{q\partial_x h\partial_z h}{h^2} - \frac{\partial_x p\partial_x h}{h} - \frac{43}{16}\frac{\partial_z q\partial_x h}{h} - \frac{13}{16}\frac{\partial_x q\partial_z h}{h}\\
&\left.+\frac{3}{4}\frac{p\,(\partial_x h)^2}{h^2} - \frac{23}{16}\frac{p\partial_{xx}h}{h} - \frac{73}{16}\frac{q\partial_{xz}h}{h} + \partial_{xx}p + \frac{7}{2}\partial_{xz}q\right]\\
&-\frac{5}{6}\zeta h\,\partial_z h + \frac{5}{6}h\,(\partial_{xxz} + \partial_{zzz})\,h\,.
\end{aligned}$$

Equation (2) expresses the mass conservation, and (5a,5b) express the averaged momentum balances in directions x and z, respectively. The viscous drag corresponds to the terms $\frac{5}{2}q/h^2$ in (5a) and $\frac{5}{2}p/h^2$ in (5b). As for system (1), the gravity acceleration contributes only to the streamwise momentum balance through the term $\frac{5}{6}h$ in (5a).

The *regularized model* (2,5) is fully consistent with the Benney expansion at second order [11], while the *simplified model*, corresponding to the averaging of the momentum balance equations across the layer depth assuming both parabolic velocity profiles and weights, is not. The simplified model can be recovered from the regularized one by replacing the factor $\mathcal{G}_\parallel$ by unity —or equivalently by assuming the actual order of s_i, r_i to be of higher order than ϵ, so that their derivatives can be neglected in the *complete model*.

III. Two-dimensional simulations of three-dimensional flows

In this section we perform time integrations of the regularized model (2,5). Periodic boundary conditions in both x and z directions are enforced. This allows us to make use of the good convergence properties of spectral methods. A pseudo-spectral explicit scheme has been developed, with derivatives evaluated in Fourier space and nonlinearities in physical space. The time dependence is accounted for by a fifth-order Runge-Kutta scheme, which allows us to control the error by difference with an embedded fourth-order scheme [12]. In practice, the time step is adapted to limit the relative error on each variable to 10^{-4}. The computational domain of size $L_x \times L_z$ is discretized with $M \times N$ regularly spaced grid points with coordinates $x_i = iL_x/M$ and $z_j = jL_z/N$. The three-dimensionality of the waves is evaluated through:

$$E_x(t) \equiv \frac{1}{(M-1)N}\sum_{j=1}^{N}\left(\sum_{m=1}^{M-1}|a_m(z_j,t)|^2\right)^{1/2}, \quad (6a)$$

$$E_z(t) \equiv \frac{1}{M(N-1)}\sum_{i=0}^{M}\left(\sum_{n=1}^{N-1}|b_n(x_i,t)|^2\right)^{1/2}, \quad (6b)$$

where the spatial Fourier coefficients a_m and b_n are defined by

$$a_m(z,t) = \sum_{i=1}^{M} h(x_i,z,t)\exp\left(\mathrm{i}2\pi mi/M\right), \quad (6c)$$

$$b_n(x,t) = \sum_{j=1}^{N} h(x,z_j,t)\exp\left(\mathrm{i}2\pi nj/N\right), \quad (6d)$$

and where i stands for the imaginary number. E_x and E_z are the streamwise and the spanwise energy of deformations as defined by Joo *et al.* [13].

Owing to the spatial periodicity in the streamwise direction, our simulations physically correspond to a closed flow for which the fluid leaving the downstream border of the computational domain is reinjected at the upstream boundary. The mass is therefore conserved in the domain so that the space-averaged film thickness $\langle h\rangle_X$ remains constant and is equal to the initial flat-film thickness (1 in our scaling). However, because the flow is gravity-oriented, the closed-flow condition cannot be achieved experimentally. In experiments, the flow is open and the time-averaged flow rate $\langle q\rangle_T = 1/3$ is conserved at each location on the plane. The corresponding open-flow condition for the traveling waves reads [14]

$$\langle h\rangle = \frac{1/3 - q_0}{c}. \quad (7)$$

Relation (7) shows that the averaged thickness $\langle h\rangle$ can be significantly lower than the inlet thickness, depending on the wave characteristics c and q_0. Therefore, in order to improve comparisons of our simulations to experimental data, we turn to our advantage the closed-flow condition inherent in the numerical scheme by imposing a film thickness tuned to the value obtained from (7) for 2D traveling waves at the corresponding forcing frequency, using the continuation software Auto97. Doing so ensures that we "embark" the right amount of liquid in our computational domain lying under the 2D traveling waves. Since the local flow rate varies as the cube of the local film thickness, this trick can be decisive in recovering experimental results. Thus, the development of 2D waves undergoing 3D instabilities is simulated by enforcing initial conditions in the form:

$$h(x,z,0) = \langle h\rangle + A_x\cos\left(\tfrac{2\pi n_x x}{L_x}\right) + A_z\cos\left(\tfrac{2\pi n_z z}{L_z}\right) + A_{\mathrm{noise}}\tilde{r}(x,z), \quad (8)$$

where $A_x, A_z, A_{\mathrm{noise}}$ are small amplitudes, $n_x, n_z \in \mathbb{N}$ represent the numbers of sinusoidal waves in each direction, and $\tilde{r}$ is a random function with values in the interval $[-1,1]$. The last term of (8) accounts for ambient white noise whose amplitude is set to $A_{\mathrm{noise}} = 10^{-3}$. For most of the computations, the aspect ratio of the domain is equal to unity, so $L_x = L_z \equiv L$. The value of L must be taken large enough to be representative of complex flow dynamics. The general form of (8) enables us to explore a wide range of experimental results on 3D waves emerging from 2D waves. In the following, we consider 3D modulations of γ_2 waves (*i.e.* positive and fast waves). In practice we are interested in domains with lengths fitting an integer number of the traveling waves under consideration.

We thus consider the experimental conditions investigated by Park & Nosoko [8] who observed 3D wave patterns emerging from 2D waves of γ_2-type. Parameter values corresponding to the different numerical experiments are given in table I, where R is the Reynolds number and f(Hz) the forcing frequency. Park & Nosoko have imposed a periodic modulation in the spanwise direction, which enforced the selection of synchronous patterns (*i.e.* in-phase modulations). These authors placed an array of regularly spaced needles with period λ_z^{ndl} (given in mm) at the inlet; k_z is thus the corresponding dimensionless wavenumber. Finally, k, c and $\langle h\rangle$ given in table I are, respectively, the dimensionless wavenumber, the phase speed and the averaged thickness of the corresponding 2D traveling waves.

Figure 1 shows snapshots for parameter set #1. Initial spanwise modulations of period $\lambda_z^{\mathrm{ndl}} = 10$ mm ($n_z = 6$)

TABLE I

PARAMETERS OF THE SIMULATIONS CORRESPONDING TO THE EXPERIMENTS BY PARK & NOSOKO [1] FOR A VERTICAL PLANE AND PURE WATER AT 25°C ($\Gamma = 3375$).

#	R	f	$\lambda_z^{\rm ndl}$	k	c	$\langle h \rangle$	k_z
1	20.7	15	10	0.346	0.900	0.899	0.699
2	20.9	19	30	0.472	0.832	0.911	0.233
3	40.8	19	20	0.385	0.714	0.912	0.377
4	59.3	17	20	0.313	0.630	0.955	0.393

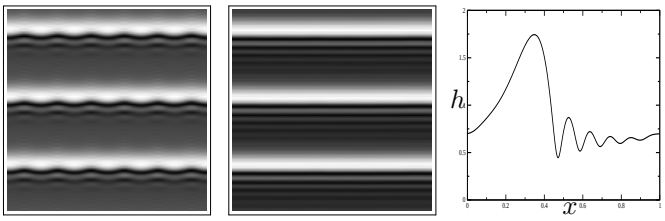

(a) $t = 27$ (b) $t = 172$ (c) $L_x = 2\pi/k$

Fig. 1. (a,b) Snapshots of the film free surface at two different times computed with the regularized model (2,5) and for parameter set #1 (see table I). Initial conditions are: $A_x = 0.2$, $A_z = 0.05$, $A_{\rm noise} = 10^{-3}$, $n_x = 3$, $n_z = 6$ and $L = 2n_x\pi/k$. The computational domain is 60×60 mm with 128×128 grid points. Bright (resp. dark) zones correspond to elevations (resp. depressions). (c) 2D wave profile of (b).

are quickly damped, i.e. $E_z \to 0$, and the pattern evolves to 2D traveling waves, i.e. $E_x \to cst$, the profile of which is given in figure 1(c). It corresponds to a γ_2 wave with a large hump preceded by capillary waves, since when the forcing frequency is small, the γ_1 slow waves are not observed and the linear inception region is immediately followed by the formation of fast γ_2 waves. Such genuine 2D waves have been observed by Park & Nosoko [8] in the right part of their test section (see figure 2(a)) while in the left part, they additionally observed large spanwise modulations with a wavelength of about $3\lambda_z^{\rm ndl}$. We recovered these modulations (not shown here) by increasing the period $\lambda_z^{\rm ndl}$ to 30 mm ($n_z = 2$). However, they also decayed (with $E_z \to 0$) but at a much smaller rate indicating that the wavelength $\lambda_z = 3$ cm is close (but still below) the cut-off wavelength for spanwise instability.

Figure 2(b) shows an experimental picture for approximately the same Reynolds number but for a higher frequency than for figure 2(a) (parameter set #2) and figure 3 shows the results of simulations with the regularized model (2,5). In this case, the initial spanwise modulation is unstable and figures 3(a,b) give patterns equivalent to those observed experimentally. Wishing to compare the evolution in time of our simulations to the evolution in space of experimental waves, we need a way to convert locations in the laboratory frame to dimensionless time in our computations. This is done by exploiting the fact that a wave traveling at speed c reaches location x at time x/c. The speeds of the 2D traveling waves corresponding to the

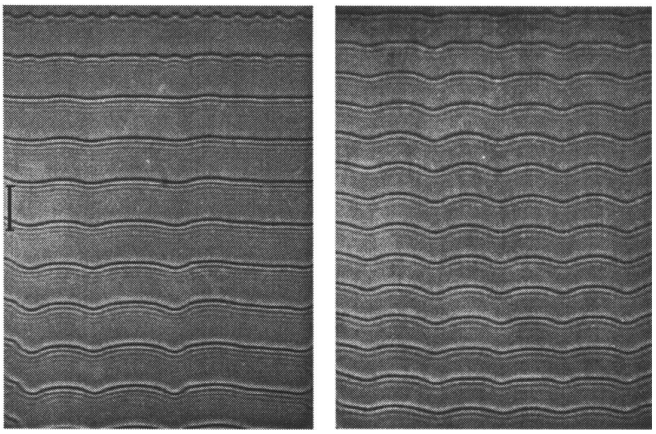

(a) (b)

Fig. 2. Experimental pictures by Park & Nosoko (figure 7a,b in [1]). (a) $R = 20.7$, $f = 15$ Hz and $\lambda_z^{\rm ndl} = 10$ mm; (b) $R = 20.9$, $f = 19$ Hz and $\lambda_z^{\rm ndl} = 30$ mm.

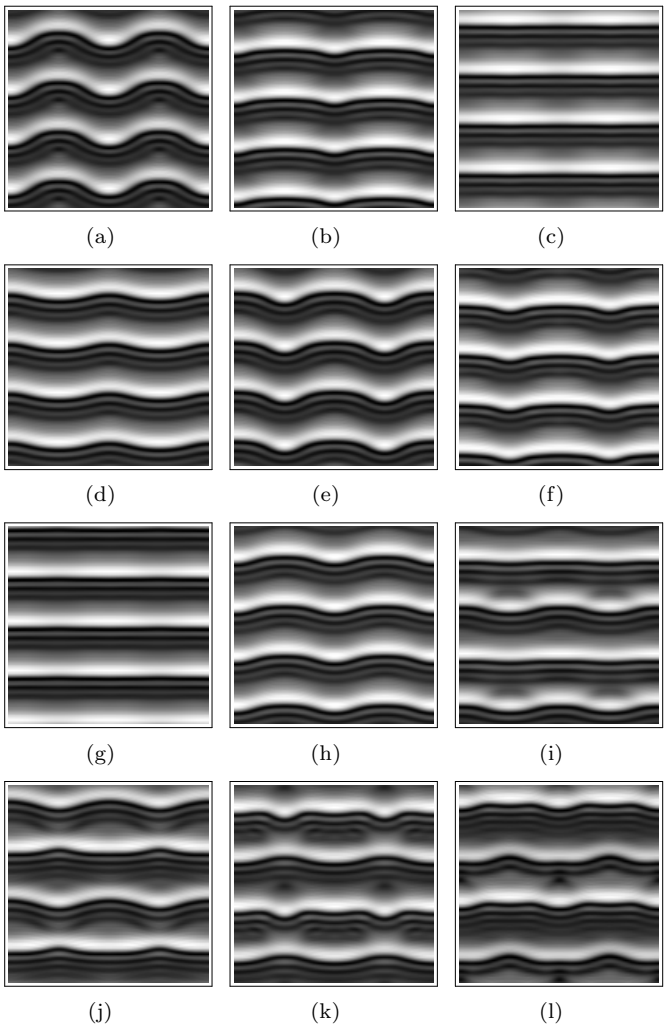

(a) (b) (c)
(d) (e) (f)
(g) (h) (i)
(j) (k) (l)

Fig. 3. Simulations for the parameter set #2. See the caption of figure 1, except for $n_x = 4$ and $n_z = 2$. Corresponding times are given in figure 4.

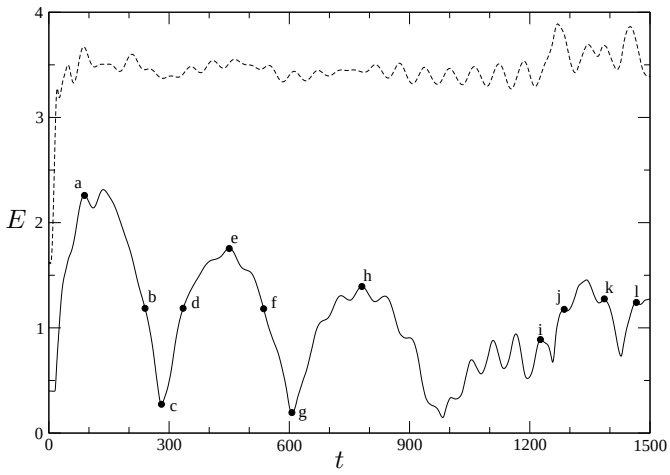

Fig. 4. Deformation energies (see equations 6) for simulations of set #2: dashed line for E_x and solid line for E_z. Letters refer to the snapshots of figure 3.

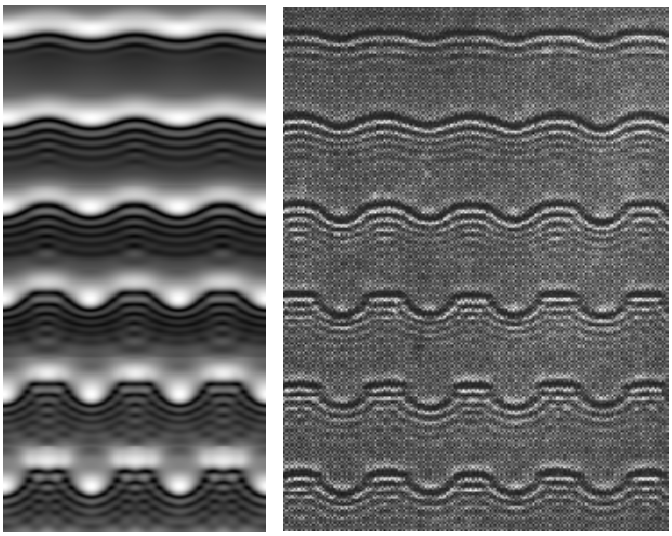

(a) Simulation (b) Experiment

Fig. 5. (a) Snapshots of the film free surface for set #3. Parameters are given in the caption of figure 1, except for $n_x = n_z = 3$. The computational domain is 60×60 mm with 256×256 grid points. (b) Experimental picture by Park & Nosoko (figure 7*c* in [1]). $R = 40.8$, $f = 19$ Hz and $\lambda_z^{\mathrm{ndl}} = 20$ mm.

experimental conditions have thus been computed using AUTO97. The test section in the experiments is 20 cm long which corresponds approximately to 200 dimensionless time units in our simulations. Having run the simulation for a much longer time (1500 time units), we have observed time oscillations of the spanwise modulations. Figure 4 shows that the energy of spanwise deformations E_z varies with a periodicity of about 300 time units. The region of the experimental domain corresponding to $t \approx 300$ is thus located beyond the test section, which explains why Park & Nosoko could not observe that behavior. Oscillations of shorter period (about 60 time units) can also be noticed, more pronounced for E_x than for E_z in figure 4. Their amplitudes are small at the beginning so that it is difficult to observe their effects on the 3D wave pattern. However, they grow for $t > 900$ where they begin to influence the evolution of the pattern in a complex way as illustrated by the last panels (*i*-*l*) of figures 3. As time is running, spanwise modulations of the fronts depart more and more from their initial sinusoidal shape. The fronts start to develop rounded tips separated by flat regions. At least two symmetry breakings can be observed. The first one corresponds to a streamwise period doubling of the modulated fronts triggered by a 2D subharmonic instability, since two identical fronts are observable in panel (*i*) instead of four in panel (*h*). The second one corresponds to the development of a phase shift of π observable between the tips of two successive fronts (compare panel *l* to panel *k*).

Simulation results for a larger Reynolds number $R = 40.8$ are presented in figure 5(a) (parameter set #3). The wavelength of the spanwise initial modulations was chosen to correspond exactly to the streamwise perturbations thus $n_x = n_z = 3$. As for $R = 20.9$, we first observed sinusoidal spanwise modulations of the 2D waves. However, they rapidly evolved into rugged modulations, made of nearly flat backs and rounded fronts. The pattern then saturated for a while (at least during 30 time units), traveling downstream in a quasi-steady state. A large number of mesh points (256×256) was here necessary to accurately capture details of the film dynamics, like for instance the checkerboard interference pattern of the capillary waves preceding the flat zones. The resemblance with the experimental findings shown in figure 5(b) is excellent and confirm the ability of the regularized model to capture complex wave dynamics of falling films up to moderate Reynolds numbers. The occurrence of these rugged-modulated waves can also be observed at smaller Reynolds number when the streamwise and spanwise initial perturbations have comparable wavelengths, as confirmed by our numerical experiments corresponding to the parameter set #2 with $n_x = n_z = 3$ (not shown).

Above $R \approx 40$, Park & Nosoko observed a breaking of the modulated fronts leading to horseshoe-like waves. Simulation results for $R = 59.3$ are presented in figure 6(a) (parameter set #4) and confronted to the experimental picture in figure 6(b). Due to computational limitations, the computational domain was this time limited to only one and two wavelengths in the streamwise and spanwise directions respectively ($n_x = 1$ and $n_z = 2$). As compared to $R = 40.8$, the rugged modulations develop faster and do not saturate. Instead, the curve bulging of the wave front continuously expand into horseshoe-shapes, reducing the span of the flat parts at the back. As time proceeds, the legs of the horseshoes extend and split off into dimples, in close agreement with experimental observations.

IV. Conclusions

In most cases, asymptotic expansions are poorly converging and the Benney expansion is no exception to this rule [14]. If an improvement of the accuracy is achieved by increasing the order of the approximation, this is at the cost

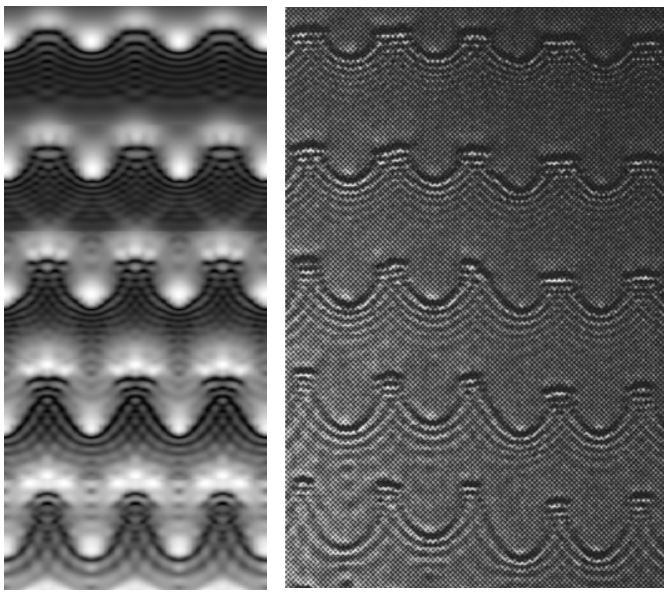

(a) Simulation (b) Experiment

Fig. 6. (a) Snapshots of the film free surface for set #4. Parameters are given in the caption of figure 1, except for $n_x = 1$ and $n_z = 2$. The computational domain is 25×40 mm with 256×256 grid points. (b) Experimental picture by Park & Nosoko (figure $7d$ in [1]). $R = 59.3$, $f = 17$ Hz and $\lambda_z^{\rm ndl} = 20$ mm.

of an increased complexity and a reduction of the range of parameters for which comparisons with DNS and experiments are improved. Padé approximant techniques are well known for their ability to extend the radius of convergence of algebraic series. In the case of 2D flows, Ooshida's application of this idea to the Benney expansion remedies the unphysical occurrence of finite-time blow-up of solutions to the Benney equation but a quantitative agreement cannot be achieved with experiments for δ of order unity or larger [15].

Focusing on the treatment of inertia terms, our algebraic regularization procedure enabled us to obtain a three-equation model which is fully consistent with the Benney expansion up to second-order. The use of a kind of algebraic preconditioner makes its application much simpler than Ooshida's approach based on differential operators. Our hope is that this Padé-like strategy might be useful for different related problems in lubrication theory for which a careful treatment of inertial effects are of importance, e.g. film flows where mass and heat transfer are involved, films down fibers, and roll waves.

Simulations presented in this work have proved the ability of our regularized model to capture the complex dynamics of surface waves in a large range of Reynolds numbers, as supported by the comparisons to the available experimental data [8]. In particular, the rugged-modulated waves as well as the horseshoe-like 3D solitary waves observed in experiments are all reliably recovered in our simulations. Even the interference of the capillary waves preceding the rugged-modulated fronts are observable in our simulations.

Notice however that the transition from modulated waves to horseshoe-like solitary waves is far from being understood. An exploration of the different wave regimes in parameter space will be the subject of a future study.

Acknowledgments

This study was partly funded by a grant from both French and Belgium research agencies (CNRS/CGRI-FNRS cooperation agreement). B. S. acknowledges funding from the European Commission through the Marie-Curie Training Center.

Appendix

I. Projection of the velocity

The streamwise velocity profile is defined as

$$u = 3\frac{q - s_1 - s_2}{h} g_0\Big(\frac{y}{h}\Big) + 45 s_1\, g_1\Big(\frac{y}{h}\Big) + 210 s_2\, g_2\Big(\frac{y}{h}\Big)\ , \quad (9)$$

where the polynomials read (details are given in [10]):

$$\begin{aligned} g_0(\bar{y}) &= \bar{y} - \tfrac{1}{2}\bar{y}^2\,, \\ g_1(\bar{y}) &= \bar{y} - \tfrac{17}{6}\bar{y}^2 + \tfrac{7}{3}\bar{y}^3 - \tfrac{7}{12}\bar{y}^4\,, \\ g_2(\bar{y}) &= \bar{y} - \tfrac{13}{2}\bar{y}^2 + \tfrac{57}{4}\bar{y}^3 - \tfrac{111}{8}\bar{y}^4 + \tfrac{99}{16}\bar{y}^5 - \tfrac{33}{32}\bar{y}^6\,. \end{aligned}$$

The spanwise velocity profile w is projected on the same basis of polynomials and obtained from (9) under the change $\{q \to p, s_1 \to r_1, s_2 \to r_2\}$.

References

[1] Piotr Leonidovich Kapitza, "Wave flow of thin layers of a viscous fluid," in *Collected papers of P.L. Kapitza*, D. Ter Haar, Ed., pp. 662–689. Pergamon, 1948, original paper: Zh. Ekper. Teor. Fiz. **18**, 3-28 (in Russian).

[2] B. Scheid, C. Ruyer-Quil, and P. Manneville, "Wave patterns in film flows: Modelling and three-dimensional waves," *In Press to J. Fluid Mech.*, 2006.

[3] G.J. Roskes, "Three-dimensional long waves on a liquid film," *Phys. Fluids*, vol. 13, pp. 1440–1445, 1969.

[4] R. W. Atherton and G. M. Homsy, "On the derivation of evolution equations for interfacial waves," *Chem. Engng Com.*, vol. 2, pp. 57–77, 1976.

[5] R.V. Roy, A.J. Roberts, and M.E. Simpson, "A lubrication model of coating flows over a curved substrate in space," *J. Fluid Mech.*, vol. 454, pp. 235–261, 2002.

[6] S. V. Alekseenko, V. Y. Nakoryakov, and B. G. Pokusaev, *Wave flow of liquid films.*, Begell House, 1994.

[7] H.-C. Chang and E. A. Demekhin, *Complex wave dynamics on thin films*, Elsevier, 2002.

[8] C. D. Park and T. Nosoko, "Three-dimensional wave dynamics on a falling film and associated mass transfer.," *AIChE J.*, vol. 49, no. 11, pp. 2715–2727, 2003.

[9] H.-C. Chang, E. A. Demekhin, and D. I. Kopelevitch, "Nonlinear evolution of waves on a vertically falling film.," *J. Fluid Mech.*, vol. 250, pp. 433–480, 1993.

[10] Christian Ruyer-Quil and Paul Manneville, "Improved modeling of flows down inclined planes," *Eur. Phys. J. B*, vol. 15, pp. 357–369, 2000.

[11] D. J. Benney, "Long waves on liquid film.," *J. Math Phys.*, vol. 45, pp. 150–155, 1966.

[12] W.H. Press, S.A. Teukolsky, W.T. Vetterling, and B.P. Flannery, *Numerical recipes in C - The Art of Scientific Computing*, Cambridge University Press (New York), second edition, 1992.

[13] S.W. Joo and S.H. Davis, "Instabilities of three-dimensional theory viscous falling films," *J. Fluid Mech.*, vol. 242, pp. 529, 1992.

[14] B. Scheid, C. Ruyer-Quil, U. Thiele, O.A. Kabov, J.C. Legros, and P. Colinet, "Validity domain of the Benney equation including Marangoni effect for closed and open flows," *J. Fluid Mech.*, vol. 527, pp. 303–335, 2005.

[15] Takeshi Ooshida, "Surface equation of falling film flows which is valid even far beyond the criticality.," *Phys. Fluids*, vol. 11, pp. 3247–3269, 1999.